State-selective Differential Cross Section Measurements for the One-electron Capture Process in O^{2+} – He and N^{2+} – He Systems at E_{lab} = 48 eV

Yoh Itoh*

Physics Laboratory, Faculty of Science, Josai University, Saitama 350-0295, Japan

(Received)

Performing high-angular-resolution measurements, we studied the relative state-selective differential cross sections (DCSs) for the following reaction channels: $O^{2+}(2s^22p^2\ ^3P) + He\ (1s^2\ ^1S) \rightarrow O^+(2s^22p^3\ ^2P) + He^+(1s\ ^2S) + 5.52$ eV and $N^{2+}(2s^22p\ ^2P) + He\ (1s^2\ ^1S) \rightarrow N^+(2s^22p^2\ ^3P) + He^+(1s\ ^2S) + 5.01$ eV. The collision energy in the laboratory frame, E_{lab}, was 48 eV. We applied a two-state semiclassical analysis based on ab initio potentials for the OHe^{2+} and NHe^{2+} systems. We concluded that the rainbow scattering and Stückelberg oscillations characterize the observed DCS structure in the O^{2+} – He case. In contrast, in the N^{2+} – He case, the prominent peak of the DCS at an angle of 0° is due to the forward glory scattering. Rainbow structures are also seen. The measured DCS was deduced to appear as the envelope of rapid oscillations in the theoretically calculated DCS.

1. Introduction

It is widely accepted that inelastic processes in low-energy collisions are primarily caused by transitions through avoided crossings in relevant interaction potentials. It is also recognized that reactions occur via nonadiabatic radial and rotational couplings around the crossing points, and the former is dominant in low-energy collisions. [1)] Charge-transfer reactions also provide excellent conditions for studying state selectivity and transition probability in associated avoided crossings.

We have been studying the charge-transfer reaction[2-5)] by combining a crossed-beam apparatus with a small electron-beam ion source (EBIS) at an energy below the laboratory (lab) frame energy,

E_{lab} = 50 eV. We intended to perform state-selective differential cross section (DCS) measurements. The summary of our study is as follows. (i) We only observed the reactions starting from the ground state of projectile ions so far, because almost all the ions produced by the EBIS are electronically in the ground state. (ii) No endothermic reaction was observed, and only one or two reaction channels were open; therefore, they could be easily and accurately identified and analyzed. (iii) DCSs often showed the typical character of rainbow scattering, and forward glory scattering was observed when the interaction potential had an apparent attractive character.

The aim of the present study is to measure state-selective DCSs with high angular resolution and to identify the reasons for their structures using theoretical calculations. We previously reported results for a one-electron transfer reaction in the O^{2+} – He system below E_{lab} = 50 eV. [3] The angular resolution was not high enough for a direct comparison with the theoretical results reported by Heil and Sharma. [6] We precisely determine the DCS to make a direct comparison with the theoretical results. Then, the results in the O^{2+} – He system are compared with those of a similar system, N^{2+} – He, to provide a clear understanding of the characteristics of the DCSs in both systems.

The dominant reaction mechanism in this energy region is considered to be radial coupling, [1] which connects states with the same symmetry. Therefore, for analysis, we only consider the reaction channels that correlate the potentials with the same symmetry.

As shown above in (i), only the ground electronic state of O^{2+} ($2s^2 2p^2\ ^3P$) was produced in the ion source; then, the ^3P state of O^{2+} and the ^1S state of He ($1s^2\ ^1S$) correlate to form molecular states with the symmetries of $^3\Sigma^-$ and $^3\Pi$. Butler et al. [7] reported that the $^3\Sigma^-$ state showed no evidence of avoided crossings in OHe^{2+} potentials, and thereby excluded the reaction channels associated with this state in their work.

The following reaction channels are open for exothermic reactions:

$O^{2+}(2s^2 2p^2\ ^3P) + He(1s^2\ ^1S)$

$$\rightarrow O^+(2s^2 2p^3\ ^2P) + He^+(1s\ ^2S) + 5.52\ \text{eV}, \quad (1)$$

$$\rightarrow O^+(2s^2 2p^3\ ^2D) + He^+(1s\ ^2S) + 7.21\ \text{eV}, \quad (2)$$

$$\rightarrow O^+(2s^2 2p^3\ ^4S) + He^+(1s\ ^2S) + 10.53\ \text{eV}. \quad (3)$$

Molecular states with the $^3\Pi$ symmetry correlate with channels (1) and (2), and $^3\Sigma^-$ states correlate with channels (2) and (3). Kamber et al. [8] studied state selectivity in O^{2+} – He collisions at E_{lab} = 6 keV, and found that all channels were open, with channel (2) being the most favorable. McLaughlin et al. [9] reported a similar trend in selectivity across E_{lab} = 2 – 8 keV, noting that channel (3) became more significant as the impact energy increased. When the collision energy was lowered to E_{lab} = 60 – 200 eV, Kamber et al. [10] found that the predominant reaction pathway turned out to be channel (1). Our previous measurement [3] also indicated that only channel (1) was open below E_{lab} = 50 eV. In the rest of the present paper, we consider only reaction channel (1) and the molecular state with $^3\Pi$ symmetry in O^{2+} – He collisions.

In the case of the N^{2+} – He system, the ground electronic state of $N^{2+}(2s^2 2p\ ^2P)$ and the ^1S state of $He(1s^2\ ^1S)$ correlate to the molecular states with the symmetries $^2\Sigma^+$ and $^2\Pi$. The following reaction channels are open for exothermic reactions:

$N^{2+}(2s^2 2p\ ^2P) + He(1s^2\ ^1S)$

$$\rightarrow N^+(2s^2 2p^2\ ^1S) + He^+(1s\ ^2S) + 0.96\text{eV}, \quad (4)$$

$$\rightarrow N^+(2s^2 2p^2\ ^1D) + He^+(1s\ ^2S) + 3.12\text{eV}, \quad (5)$$

$$\rightarrow N^+(2s^2 2p^2\ ^3P) + He^+(1s\ ^2S) + 5.01\text{eV}. \quad (6)$$

Molecular state $^2\Sigma^+$ correlates to reaction channels (4) and (5), and $^2\Pi$ correlates to channels (5) and (6). The measured results of Sato and Moore [11] in the energy range E_{lab} = 0.4 to 2.0 keV showed that reaction channel (6) was the primary process, and the relative importance of channel (5)

decreased with decreasing collision energy. Sharma et al. [12] and Lennon et al. [13] also studied the state selectivity of the reactions. They indicated trends similar to those observed by Sato and Moore in comparable energy regions. Our previous study [14] revealed that only channel (6) was open at E_{lab} = 20 eV; in the present paper, we will only consider the interaction potentials with $^2\Pi$ symmetry and reaction channel (6) for N^{2+} – He collisions.

The following section outlines the experimental procedure. The measured results and the interpretation of the structure in the DCSs are presented in Sec. 3, where we compare them with semiclassically calculated DCSs based on ab initio potentials. In Sect. 4, we summarize the discussion.

2. Experimental Procedure

Details of the apparatus were described previously.[2, 3] Briefly, multiply charged ions were generated using a small EBIS based on the design of mini-EBIS by Okuno.[15] After ion production, the mass- and energy-selected ions were directed to intersect the supersonic nozzle beam at right angles. The detector system was set in an in-plane configuration.

Regarding ion beam quality, Ishii et al.[16] reported metastable ion fractions of about 3% for C^{2+} and 3.5% for O^{2+} in the ion beam produced by the mini-EBIS. Because our operating parameters, such as electron beam current (typically 10 mA), electron beam energy (1 – 2 keV), applied magnetic field (about 0.15 T), and operating gas pressures (below 10^{-7} Pa), closely matched those of Ishii et al., we therefore assume that our metastable ion percentages are similar for O^{2+} as well as for N^{2+} ions.

We recently installed two 0.2-mm-diameter pinholes, spaced 60 mm apart, between the energy selector and the collision center to enable high-angular-resolution measurements. The apertures

limit the angular divergence of the primary beam to ±0.2°.

Scattered ions were transported from the collision center to the entrance slit of the energy analyzer through a carefully shielded path to preserve scattering angle information. No ion optics were used.

The energy of the scattered ions and the scattering angle were measured simultaneously using a 90° electrostatic cylindrical analyzer and a two-dimensional (2D) position-sensitive detector (PSD) system. The acceptance angle of the detector was about ±1.5°. This 2D-PSD was composed of two microchannel plates (MCPs) and an anode based on the modified backgammon method with weighted coupling capacitors (MBWC). [17)]

To detect ions on the MCP while preserving the energy and angle information of the scattered particles, the space between the analyzer exit and the MCP detector was also carefully shielded. The opening area of the MCP was shielded to prevent the leakage of the electric field due to the ion-acceleration potential applied to the surface of the first MCP. This shield consisted of 50 wires, each 50 μm in diameter, spaced at 1 mm intervals. It was oriented in the same direction as the detector's angular-dispersion direction, ensuring no disturbance to the angular-spectrum measurement. When the energy determination of the scattered ions was the primary focus of the measurements, the shielding wire was rotated 90° to align with the energy-dispersion direction.

The charge collected by four strips of the MBWC anode was converted to voltage pulses proportional to the amount of charge by standard electronics and fed to four analog-to-digital converters (ADCs). The ADC chip (ADC2318) used has a resolution of 12 bits and a constant conversion time of 1.2 μs.[18)] These features were well suited to the present measurements, and we could build a data-acquisition system using four ADCs in coincidence without much difficulty.

The position signals were calculated and stored by a personal computer (PC). Energy and

position spectra were displayed during the measurement, and raw data were also saved in list mode on the PC. The data could be processed as needed after the measurement was completed, for example, by using different noise discrimination levels.

3. Results and Discussion

3.1 Calibration: DCS measurements for elastic scattering in $^3He^+ - {}^4He$

The calibrations for the collision energy and scattering angle were performed by comparing the presently measured results with the calculation. We measured the relative DCS for elastic scattering in the $^3He^+ - {}^4He$ system for this purpose. The $^3He^+$ ions were applied because the angular dependence of the theoretical DCS was reported to be simpler than that of the symmetric system $^4He^+ - {}^4He$ (see, for example, Figs. 1 and 2 in Ref. 19).

The primary-beam energy was determined as follows: first, the energy of the primary beam was decelerated to almost 0 eV, with the beam intensity monitored; then, an additional accelerating voltage was applied to the ion source to determine the beam energy. The accuracy of the beam-energy determination was estimated to be ±1 eV.

An example of the measured spectrum is shown in Fig. 1. The collision energy was determined to be E_{lab} = 28 ± 1 eV. This spectrum was obtained by setting the detector at 4.5° relative to the incident ion-beam direction. This angle region corresponds to the rainbow-scattering angle.[20] The results are shown in a three-dimensional (3D) graph, i.e., the signal counts are displayed as a function of ion energy and scattering angle. The accumulation time was about 40 h.

In Fig. 1, many peaks are observed on the shoulder of a broad peak, and the angular distance between the peaks corresponds to an angle of about 0.5° in the lab frame. The relative DCS in the lab frame was determined by integrating the signal counts shown in Fig. 1 along the ion energy at

each scattering angle. The DCS obtained in the lab frame was converted to that in the center-of-mass (cm) frame using the procedure reported by Morse and Bernstein.[21] The measured DCS in the cm frame is shown in Fig. 2, as well as the calculated DCS, obtained as shown below, for comparison.

Following the procedures for DCS calculation reported by Olson and Mueller,[19] we computed the DCS and compared it with our experimental results. This comparison is also aimed at evaluating the angular resolution of our current setup. Atomic units (a.u.) are used unless otherwise indicated. As the collision system is $^3He^+ - {}^4He$, which lacks nuclear symmetry, the DCS for elastic collisions is expressed as

$$\frac{d\sigma}{d\Omega} = \frac{1}{4}\left| f_{\mathrm{u}}(\theta) + f_{\mathrm{g}}(\theta) \right|^2 \qquad (7)$$

and

$$f_{\mathrm{u,\,g}}(\theta) = \frac{1}{2ik}\sum_l (2l+1)\left[\exp(2i\eta_l^{\mathrm{u,\,g}}) - 1\right] P_l(\cos\theta) \quad , \qquad (8)$$

where $f_{\mathrm{u,\,g}}(\theta)$ is the scattering amplitude at the cm frame angle θ, from the ungerade potential $V_{\mathrm{u}}(r)$ or the gerade potential $V_{\mathrm{g}}(r)$, k is the wavenumber of the collision system, l is the angular momentum quantum number, and $P_l(\cos\theta)$ is the lth-order Legendre polynomial.

We applied the numerical values of $V_{\mathrm{u,g}}(r)$ reported by Xie et al.[22] and fitted them to $V_{\mathrm{u}}(r) = 0.09092\,[e^{-2.2112\,(r-2.042)} - 2\,e^{-1.1056\,(r-2.042)}]$ and $V_{\mathrm{g}}(r) = 1.3105\,e^{-(r-1.0)/0.55995} + 0.24106\,e^{-(r-1.0)/0.88358}$. The phase shifts $\eta_l^{\mathrm{u,g}}$ were calculated using a standard WKB method, and the angular momentum l up to 2000 was taken into account. We found that the calculated DCS at $E_{\mathrm{lab}} = 29$ eV best matches the measured DCS. This collision energy discrepancy is within the estimated experimental error. The measured relative DCS was scaled to the theoretical one at $\theta \sim 0.155$ rad. No further adjustment was made. The calculated DCS shows a broad rainbow structure

superimposed with rapid oscillations. The origin of such oscillations is mainly the interference of the scattered $^3He^+$ ions by the $V_u(r)$ potential, [19] which has a well of about 2.5 eV.

The angular resolution of the present setup was estimated to be about 0.25° (FWHM) by measuring the angular width of the primary beam. The theoretical DCS convoluted under the present experimental conditions is shown in Fig. 2(b). The agreement between the measured and calculated results, shown in Figs. 2(a) and 2(b), is satisfactory; the present experimental procedures for determining the ion energy and scattering angle are adequate. The improved angular resolution allows for the separation of two peaks in the DCS that are spaced by 0.5° or less in the lab frame.

3.2 Measured results for O^{2+} – He

In Fig. 3, the measured DCS for the one-electron transfer process in the lab frame of the O^{2+} – He system is shown. The collision energy is E_{lab} = 48 eV. The DCS was determined by the same procedure as that adopted for the elastic scattering in He^+ – He, shown in Sect. 3.1. The previously reported DCS at E_{lab} = 50 eV [3] is also shown in this figure. Both results are scaled to unity at around θ_{lab} = 2°.

The energy spectrum of the scattered ions was identical to that previously reported. [3] We again assigned the signals to the following reaction channel: $O^{2+}(2s^2 2p^2\ ^3P) + He(1s^2\ ^1S) \rightarrow O^+(2s^2 2p^3\ ^2P) + He^+(1s\ ^2S) + 5.52$ eV. The positions of the peaks around θ_{lab} = 2° agree well with each other within the experimental error. While the previous result shows a broad structure with some undulations, the present DCS clearly shows four peaks at θ_{lab} = 2.3, 3.8, 5.4, and 8.0°.

3.3 Measured results for N^{2+} – He

In Fig. 4, the energy spectrum of the scattered N^+ ions created by the one-electron capture

process in the N^{2+} – He system at E_{lab} = 48 eV is shown. This spectrum was obtained by integrating all ion signals scattered between 0 and 0.5° in the 2D spectrum. The energy width of the primary beam was estimated to be 0.4 eV (FWHM). The arrow in Fig. 4 indicates the position of the ion energy corresponding to channel (5). We observed no significant signal at around this energy and concluded that only reaction channel (6) is open at this collision energy.

The measured relative DCS in the lab frame for the N^{2+} – He system is shown in Fig. 5. The peak value is scaled to unity. We observe a significantly different angular dependence of the DCS compared with that in the O^{2+} – He system. The DCS exhibits very strong forward-scattering characteristics at around the angle of 0°, a shoulder at around θ_{lab} = 0.8°, and two prominent peaks at θ_{lab} = 1.5 and 3.0°.

3.4 Analysis based on semiclassical calculations

The interaction potentials used in our analysis are shown in Fig. 6. The initial channel for the O^{2+} – He collision is $3^3\Pi$ and the charge-transfer channel is $2^3\Pi$. For the N^{2+} – He system, the initial channel is $2^2\Pi$ and the final channel is $1^2\Pi$. We use subscripts 1 and 2 hereafter to refer to the initial and final states, respectively. Regarding the O^{2+} – He system, we used the ab initio potential values reported by Butler et al. [7] and fitted them to appropriate functions. Specifically, for the $3^3\Pi$ state, $V_1(r)$ is approximated by a 10^{th}-order polynomial for $r \leq 5.85$, and $V_1(r) = 0$ for $r > 5.85$. About the $2^3\Pi$ state, $V_2(r)$ is approximated by a 14^{th}-order polynomial for $r \leq 7.0$, and for $r > 7.0$, $V_2(r)$ is fitted to $V_2(r) = 1 / r + c_0 / r^2 + c_1 / r^3 + c_2 / r^4 - 0.2029$, where c_n are fitting parameters. An arbitrary repulsive potential was added to the $2^3\Pi$ state to consider only the transition around the crossing radius (R_c) of ~ 5.13, in the following subsections.

For the N^{2+} – He potential, the values reported by Itoh and Ohtsuki [14] were applied. These

values agreed well with those reported by Lafyatis et al. [23] and Sun et al.[24] The $2^2\Pi$ state is approximated by a 13th-order polynomial for $r \leq 7.0$, and $V_1(r) = 0$ for $r > 7.0$. The $1^2\Pi$ state is fitted to a 13th-order polynomial for $r \leq 7.56$, and for $r > 7.56$, $V_2(r) = 1 / r + c_0 / r^2 + c_1 / r^3 + c_2 / r^4 - 0.1841$.

In the study on DCS calculation by Heil and Sharma, [6] they applied quantum mechanical procedures that accounted for all three potentials with the $^3\Pi$ symmetry calculated by Butler et al.[7] They provided some semiclassical interpretations of the features of their calculated DCSs, but also stated that the two-state model could not be applied because these potentials are strongly coupled. However, our measured results showed that only channel (1) is open. Therefore, it may be worthwhile to apply the two-state approximation to calculate the DCS to analyze the measured results.

We used the semiclassical procedures reported by Danared and Bárány [25] and Bárány and Crothers. [26] The calculation procedure is as follows.

The DCS for the charge-transfer reaction is expressed as

$$\frac{d\sigma}{d\Omega} = \frac{k_2}{k_1}\left|f_{12}(\theta)\right|^2 , \tag{9}$$

where k_1 is the wavenumber of the incoming particle and k_2 is that of the outgoing one. The scattering amplitude $f_{12}(\theta)$ is given by the partial-wave sum:

$$f_{12}(\theta) = \frac{1}{2i(k_1 k_2)^{1/2}} \sum_l (2l+1)\, S_{12} P_l \cos(\theta) . \tag{10}$$

The S-matrix element is expressed as

$$S_{12} = -2i\left[\, p(1-p)\right]^{1/2} \sin(\sigma + \phi) \cdot e^{i(\eta_1 + \eta_2)} , \tag{11}$$

$$p = e^{-2\delta} \quad , \tag{12}$$

where p is the nonadiabatic transition probability at a single crossing, η_1 and η_2 are the semiclassical phase shifts for elastic scattering on the adiabatic potentials V_1 and V_2, and

$$\phi = -\delta/\pi + (\delta/\pi)\log(\delta/\pi) - \arg\Gamma(i\delta/\pi) - \tfrac{1}{4}\pi \quad . \tag{13}$$

Here, Γ is the gamma function.

The parameters σ and δ, which appear in Eqs. (11) and (12), were determined as follows. Since the slopes of the diabatic potentials relevant to the reaction at the crossing point are opposite to each other, we should apply the theory of nonadiabatic tunneling to the transition. To perform the calculation according to Zhu and Nakamura's theory, it is necessary to determine the parameters a^2 and b^2 from the adiabatic potentials.[27, 28] In our case, the top and bottom of the potential curves are not sufficiently clear to derive these parameters (see Fig. 6). Therefore, we determined the parameters σ and δ directly from the complex integral:

$$\sigma + i\delta = \int_{T_2}^{R^*} k_2(r)\,dr - \int_{T_1}^{R^*} k_1(r)\,dr, \tag{14}$$

and

$$k_{1,2}(r) = \sqrt{{k_{1,2}}^2 - (l+1/2)^2 / r^2 - 2\mu V_{1,2}(r)} \,, \tag{15}$$

where T_1 and T_2 are the classical turning points, R^* is the complex crossing point that satisfies $V_1(R^*) = V_2(R^*)$, and μ is the reduced mass of the system.

The complex crossing point was evaluated to be located at 5.125 + 0.407 i for the O^{2+} – He system and at 5.627 + 0.639 i for the N^{2+} – He system. The Coulomb interaction becomes the primary interaction between the charge-transferred projectile and the target ion in the final state. We introduced a cutoff for the Coulomb interaction at an appropriate distance to apply the conventional

WKB method to the phase-shift calculations.[29] We checked the effect of the cutoff distance on the DCSs and determined that 200 a_0 is appropriate for both systems, where a_0 is the Bohr radius. We repeated the DCS calculations for the He^+ – Ne system reported by Olson and Smith,[30] and for the C^{4+} – He system studied by Danared and Bárány[25] to verify that our computing procedures were accurate.

3.5 Calculated results for O^{2+} – He

The calculated and measured DCSs for the reaction $O^{2+}(2s^2 2p^2\ ^3P) + He\ (1s^2\ ^1S) \rightarrow O^+(2s^2 2p^3\ ^2P) + He^+(1s\ ^2S) + 5.52$ eV at $E_{lab} = 48$ eV are shown in Fig. 7. The solid curve shows the present calculated results. The circles show the measured DCS converted to the cm coordinate, scaled to the present calculated value at approximately $\theta = 0.18$ rad. Comparing our result with the DCS calculated by Heil and Sharma,[6] we note that good agreement is achieved. Both the computed results perfectly reproduce the peak positions of the measured DCS. However, the absolute values for the DCSs of our calculation differ significantly from those of Heil and Sharma, especially for the first peak at about $\theta = 0.18$ rad.

One possible reason for this discrepancy is the different transition probability values, p, used in the calculations. When Gargaud et al.[31] compared their theoretical cross sections with those of Heil and Sharma, they explained the difference in theoretical value to be the result of a different coupling matrix element, V_{12}, used in the calculations. The coupling matrix element directly concerns the transition probability; for example, the Landau–Zener formula shows that $p = \exp[-2\pi V_{12}^{\ 2} / (v_r \cdot \Delta F)]$, where v_r is the radial velocity of the scattered particle and ΔF is the slope difference of the relevant diabatic potentials. V_{12}, v_r, and ΔF are evaluated at the crossing point, R_c.

In our calculation, we determine the transition probability using Eq. (12), i.e., $p = \exp(-2\delta)$. We noted that the positions of the complex crossing points, R^*, are significantly affected by the accuracy with which the fitted functions reproduce the ab initio values of the relevant potentials. We found that in Eq. (14), σ is less sensitive to the location of R^*, whereas δ is highly dependent on it. As δ determines the transition probability, the magnitude of the cross sections is significantly altered; in contrast, σ specifies the oscillatory structure in the S-matrix [see Eq. (11)]. ϕ is also a function of δ. However, it negligibly depends on the angular quantum number l over the region concerned. Therefore, it is suggested that when the transition probability is altered by the change in V_{12} or by the change in R^*, the absolute value of the DCS is affected significantly. In contrast, the angular dependence of the DCS changes negligibly. This point is discussed again in the following Sect. 3.7.2, using the concept of deflection functions.

For the fourth peak located at about $\theta = 0.6$ rad, the DCS calculated by Heil and Sharma showed a rapid oscillation, which was absent in our calculation. Although the measured data has a large margin of error, it shows a similar trend to the results obtained by Heil and Sharma. This point will also be discussed in Sect. 3.7.2.

3.6 Calculated results for N^{2+} – He

The calculated and measured DCSs for the reaction $N^{2+}(2s^2 2p\ ^2P) + He \rightarrow N^{+}(2s^2 2p^2\ ^3P) + He^{+} + 5.01$ eV at $E_{lab} = 48$ eV are shown in Fig. 8. The solid curve represents the calculated results and the circles show the measured DCS converted to the cm coordinate. The measured DCS was scaled to the calculated value at about $\theta = 0.2$ rad. Many fine oscillations are observed in the calculated DCS; the angular difference of the peaks is about 0.01 rad, corresponding to about 0.15° in the lab frame. The angular difference between the oscillations is much smaller than the angular resolution

of the present settings, about 0.25° (FWHM) in the lab frame; hence, the measured DCS appears as an envelope of the oscillating theoretical values. The broken curve in Fig. 8 shows the calculated values convoluted under the present experimental conditions. The convoluted values well reflect the features of the measured DCS: the forward peak, the shoulder, and two prominent peaks. The origin of the structures in the DCS will also be discussed in the following Sect. 3.7.3 using the deflection functions.

3.7 Semiclassical deflection functions

3.7.1 Deflection functions for curve-crossing collisions

To understand the origin of the observed structures in DCSs, it is advantageous to extract information about classical trajectories from the results of the semiclassical calculation shown above. The deflection function, i.e., the deflection angle Θ as a function of the impact parameter b, provides a comprehensive understanding of DCS data. Generally, the scattering angle is given by $\theta = |\Theta|$.

We referred to the study by Bárány [32] on deflection functions for curve-crossing collisions. The reported formulae for the deflection functions are

$$\Theta_{+} = \frac{d}{dl}(\eta_1 + \eta_2 + \phi + \sigma) \qquad (16)$$

and

$$\Theta_{-} = \frac{d}{dl}(\eta_1 + \eta_2 - \phi - \sigma) \quad . \qquad (17)$$

The calculated deflection functions using these formulae are shown in Fig. 9 for both collision systems.

Within the diabatic picture, the upper part of the deflection function, Θ_{-}, corresponds to the

charge-transfer reaction that occurs in the incoming part of the trajectory at the first crossing. The lower half of the curve, Θ_{+}, corresponds to the reaction that occurs in the outgoing part of the trajectory at the second crossing. We observe a significant difference in deflection function between the two systems. The reason for the difference is, of course, that the relevant potentials greatly differ in the two systems.

The classical DCSs for the reaction can be calculated as [25)]

$$\frac{d\sigma}{d\Omega} = \sum_{j} \frac{b_j}{\sin\theta \cdot \left| d\Theta / db_j \right|} \cdot P(b_j), \qquad (18)$$

where b_j is the possible impact parameter that will result in the same scattering angle θ and $P(b_j)$ is the transition probability: $P(b_j) = p\ (1 - p)$. The classical DCS diverges if $d\Theta/db$ becomes zero at some angle; this is the condition for rainbow scattering. Olson and Kimura [33)] called this peak the "inelastic rainbow", analogous to the rainbow phenomenon in elastic collisions. When the scattering angle, given by $\theta = |\Theta|$, becomes zero, the classical DCS again diverges; this is forward glory scattering.

3.7.2 Analysis of the structure of DCSs using deflection functions for O^{2+} – He collisions

Because the interaction potentials, $2^3\Pi$ and $3^3\Pi$, corresponding to the reaction in the O^{2+} – He system, are almost repulsive in character, the deflection angles are always positive; thus, the DCS becomes zero for the scattering angle near 0°.

In Fig. 9, the rainbow angle in O^{2+} - He, $\theta_{R_O,}$ is seen to be 0.152 rad at $b = 4.73$. The first peak in the measured DCS is located at approximately $\theta = 0.18$ rad, which is close to this rainbow angle. Therefore, the first peak could be assigned to the rainbow peak, known as the "inelastic rainbow". There exists no marked change in deflection function; a further simple interpretation of the other

peaks is difficult. These peaks are considered to be generated by the interference of trajectories owing to reactions at the incoming and outgoing parts of the paths, resulting in the same scattering angle, i.e., Stückelberg oscillations. Note that the angular width of the fourth peak, located at around $\theta = 0.6$ rad, is broader than that of the others. This broadening might be due to the closer approach of the two deflection functions at $b \sim 3.0$, corresponding to a scattering angle of 0.6 rad, a similar effect of Young's optical experiment with a narrower slit distance.

Regarding the fourth peak in the DCS, we were unable to reproduce the rapid oscillation superimposed on the broad peak reported by Heil and Sharma. They showed their DCS in the lab frame, probably for the convenience of experimentalists. Since the projectile O^{2+} is heavier than the target He, the O^+ ions scattered backward can be observed in the forward direction in the lab frame. We also converted the calculated DCS from the cm frame to the lab frame, but the oscillation was not reproduced.

As we have considered a single crossing at $R_c \sim 5.13$, we have added an arbitrarily repulsive potential (see Fig. 6). The $2^3\Pi$ potential used in our calculation deviates from that of Butler et al. at $r < 2.4$. From the lower part of the deflection function, Θ_+, we see that the deflection angle of 0.6 rad corresponds to an impact parameter of $b \sim 3.0$. The closest approach for this condition was calculated to be 3.3. For a scattering angle of 0.8 rad, the impact parameter is 2.3 and the corresponding closest approach is 2.8; this suggests that the fitted potential used for our analysis could well describe the scattering angles smaller than 0.8 rad. The origin of the rapid oscillation is currently unclear. A two-state approximation might not be able to handle this oscillation.

The angular dependences of the DCS could be understood fairly well by the character of the deflection functions, as shown above. In Sect. 3.5, we discussed how changes in transition probability, due to changes in V_{12} or R^*, affect the absolute value of the DCS but have a negligible

effect on its angular dependence. As V_{12} is often evaluated as one-half of the potential difference between the relevant potentials at R_c, a slight change in V_{12} has negligible effects on the overall characteristics of the relevant potentials, except at around R_c. Therefore, the deflection functions will not be significantly altered by a slight change in transition probability. The agreement in the angular dependences of the DCS between our calculated value and those of Heil and Sharma can be understood as follows: changes in transition probability due to changes in V_{12} or R^* negligibly affect the deflection functions.

3.7.3 Analysis of the structure in DCSs using deflection functions for N^{2+} – He collisions

The interaction potential for the initial state $2^2\Pi$ has a very shallow well, though it is mainly repulsive. Therefore, the upper part of the deflection function, Θ_-, is always positive. In contrast, the final state $1^2\Pi$ has a remarkable well; thus, the lower part of the deflection function, Θ_+, becomes either positive or negative, depending on the impact parameters.

A very prominent feature of the measured and calculated DCSs is the strong forward scattering. This feature is clearly explained: the scattering angle θ becomes zero at the impact parameters b_{G_in} = 2.4 and b_{G_out} = 4.8 (see Fig. 9). The forward peak of the DCS is clearly identified as glory scattering.

In Fig. 9, the rainbow angle θ_{R_N} in the N^{2+} – He system is observed to be 0.227 rad at b = 3.24. The broad structure of the measured DCS observed at around θ = 0.2 rad is concluded to be inelastic rainbow scattering, and the signals at around θ = 0.05 and 0.1 rad are judged to be a supernumerary rainbow from the analogue of the DCSs in the elastic collisions.[34, 35)]

The rapid oscillations observed in the calculated DCS are due to interference. Several possible impact parameters yield the same scattering angle below the rainbow angle; for example, for b = 2.2,

2.8, and 3.9, the scattering angle is 0.15 rad in each case. Therefore, the calculated DCS exhibits rapid, complex oscillations. Among these complex oscillations, we observe clear peaks with a step size of 0.01 rad over the scattering angles of 0 and 0.14 rad. One of the probable reasons for the regular oscillations in forward scattering is the glory oscillation.[36] The angular difference $\Delta\theta$ of the glory oscillation is known to be $\Delta\theta = \pi / (b_G \cdot k)$, where b_G is the impact parameter corresponding to the glory scattering. The values b_{G_in} = 2.4 and b_{G_out} = 4.8 result in glory oscillations with frequencies of 0.01 and 0.02 rad, respectively. Both b_{G_in} = 2.4 and b_{G_out} = 4.8 can produce these angular steps; therefore, it is impossible to determine which impact parameter is clearly responsible for these oscillations.

When the scattering angle exceeds the rainbow angle, only two trajectories contribute to the same scattering angle, and pure Stückelberg oscillation begins to appear. As the scattering angle increases, the frequency of these oscillations becomes longer because the difference in impact parameter required to produce the same scattering angle decreases.

To the author's knowledge, only Hormis et al.[37] reported the DCS at the collision energy of E_{lab} = 1 keV for this reaction channel. They showed that the DCS also indicates a strong forward peak and two weak undulations at $E_{lab} \cdot \theta_{lab}$ = 400 and 850 eV°. No explanation was given for the structures. In our case, prominent structures are seen at $E_{lab} \cdot \theta_{lab}$ = 72 and 144 eV°. If similar impact parameters cause the structures observed by Hormis et al. and in the present measurement, then the structures will appear at the same $E_{lab} \cdot \theta_{lab}$ values. The origin of the structures at higher collision energy might differ from that at lower collision energy.

4. Summary

We have improved the angular resolution of the crossed-beam apparatus and measured

state-selective DCSs in the O^{2+} – He and N^{2+} – He systems at E_{lab} = 48 eV. Only the O^{2+} ($2s^2 2p^2\ ^3P$) + He ($1s^2\ ^1S$) → O^+ ($2s^2 2p^3\ ^2P$) + He^+ ($1s\ ^2S$) + 5.52 eV reaction channel is open for the O^{2+} – He system, and for the N^{2+}– He system, N^{2+} ($2s^2 2p\ ^2P$) + He ($1s^2\ ^1S$) → N^+ ($2s^2 2p^2\ ^3P$) + He^+ ($1s\ ^2S$) + 5.01eV.

We compared the measured DCS with that calculated in the O^{2+} – He system using the two-state semiclassical method with ab initio potentials. Our computed results showed good agreement with the quantum results of Heil and Shama.[6] The two-state calculation could reproduce the overall characteristics of the measured results; however, it could not fully reproduce the partially observed fine structure. The semiclassical deflection function showed that the rainbow scattering and Stückelberg oscillations characterize the observed DCS structure in the O^{2+} – He system.

The same analysis procedure was applied to the N^{2+} – He system. The calculated result showed a typical rainbow and supernumerary rainbow structure, with very rapid oscillations superimposed on them. The rapid oscillation observed in the forward scattering is temporally assigned to the glory oscillation. The angular resolution of the present setup was insufficient to separate the rapid oscillatory structures; the measured DCS showed the envelope of the calculated DCS.

The different characteristics of the DCSs in the two systems are understood to be due to the very different interaction potentials relevant to the reactions.

Acknowledgements

The author is grateful to Professor F. Koike at Sophia University for valuable suggestions on performing semiclassical calculations and for the critical reading of the manuscript. This paper is dedicated to the late Dr. Kazumasa Ohtsuki, who provided the author with his unpublished

theoretical potentials.

*yoh_itoh@nifty.com

1) B. H. Bransden and M. R. C. McDowell, *Charge Exchange and the Theory of Ion-Aton Collisions* (Clarendon Press, Oxford, 1992) Chap. 4.

2) Y. Itoh, J. Phys. Soc. Jpn, **63**, 941 (1994).

3) Y. Itoh, J. Phys. B **35**, 3217 (2002).

4) Y. Itoh, J. Phys. B **44**, 175202 (2011) [Erratum **44**, 239601 (2011)].

5) Y. Itoh, J. Phys. Soc. Jpn. **85**, 094301 (2016).

6) T. G. Heil and J. B. Sharma, Phys. Rev. A **36**, 3669 (1987).

7) S. E. Butler, T. G. Heil, and A. Dalgarno, J. Chem. Phys. **80**, 4986 (1984).

8) E. Y. Kamber, A. G. Brenton, J. H. Beynon, and J. B. Hasted, J. Phys, B **18**, 933 (1985).

9) T. K. McLaughlin, S. M. Wilson, R. W. McCullough, and H. B. Gilbody, J. Phys. B **23**, 737 (1990)

10) E. Y. Kamber, C. L. Cocke, J. P. Giese, J. O. K. Pedersen, and W. Waggoner, Phys. Rev. A **36**, 5575 (1987).

11) Y. Sato and J. H. Moore, Phys. Rev. A **19**, 495 (1979).

12) S. Sharma, G. L. Awad, J. B. Hasted, and D. Mathur, J. Phys. B **12**, L163 (1979).

13) M. Lennon, R. W. McCullough, and H. B. Gilbody, J. Phys. B **16**, 2191 (1983).

14) Y. Itoh and K. Ohtsuki, J. Phys: Conf. Ser. **163,** 012042 (2009).

15) K. Okuno, Jpn. J. Appl. Phys. **28**, 1124 (1989).

16) K. Ishii, A. Itoh, and K. Okuno, Phys. Rev. A **70**, 042716 (2004).

17) T. Mizogawa, M. Sato, M. Yoshino, Y. Itoh, and Y. Awaya, Nucl. Instrum. Methods A **387**, 395 (1997).

18) https://www.smtx.co.jp/itemenglish.html.

19) R. E. Olson and C. R. Mueller, J. Chem. Phys. **46**, 3810 (1967).

20) D. C. Lorents and W. Aberth, Phys. Rev. **139**, A1017 (1965).

21) F. A. Morse and R. B. Bernstein, J. Chem. Phys. **37**, 2019 (1962).

22) J. Xie, B. Poirier, and G. I. Gellene, J. Chem. Phys. **122**, 184310 (2005).

23) G. P. Lafyatis, K. Kirby, and A. Dalgarno, Phys. Rev. A **48**, 321 (1993)

24) Y. Sun, H. R. Sadeghpour, K. Kirby, A. Dalgarno, and G. P. Lafyatis, Int. Rev. Phys. Chem. **15**, 53 (1996).

25) H. Danared and A. Bárány, J. Phys. B **19**, 3109 (1986).

26) A. Bárány and D. S. F. Crothers, Phys. Scr. **23**, 1096 (1981).

27) C. Zhu and H. Nakamura, Chem. Phys. Lett. **274**, 205 (1997).

28) C. Zhu and H. Nakamura, J. Chem. Phys. **101**, 10630 (1994).

29) F. Koike: private communication.

30) R. E. Olson and F. T. Smith, Phys. Rev. A **3,** 1607 (1971) [Erratum **6**, 526 (1972)].

31) M. Gargaud, M. C. Bachus-Montabonel, and R. McCarrol, J. Chem. Phys. **99**, 4495 (1993).

32) A. Bárány, J. Phys. B **12**, 2841 (1979).

33) R. E. Olson and M. Kimura, J. Phys. B **15**, 4231 (1982).

34) U. Buck, H. O. Hoppe, F. Huisken, and H. Pauly, J. Chem. Phys. **60**, 4925 (1974).

35) A. Ding, J. Karlau, and J. Weise, J. Chem. Phys. **65**, 2544 (1976).

36) M. V. Berry, J. Phys. B **2**, 381 (1969).

37) W. G. Hormis, E. Y. Kamber, and J. B. Hasted, Int. J. Mass Spectrom. Ion Proc. **69**, 211 (1986).

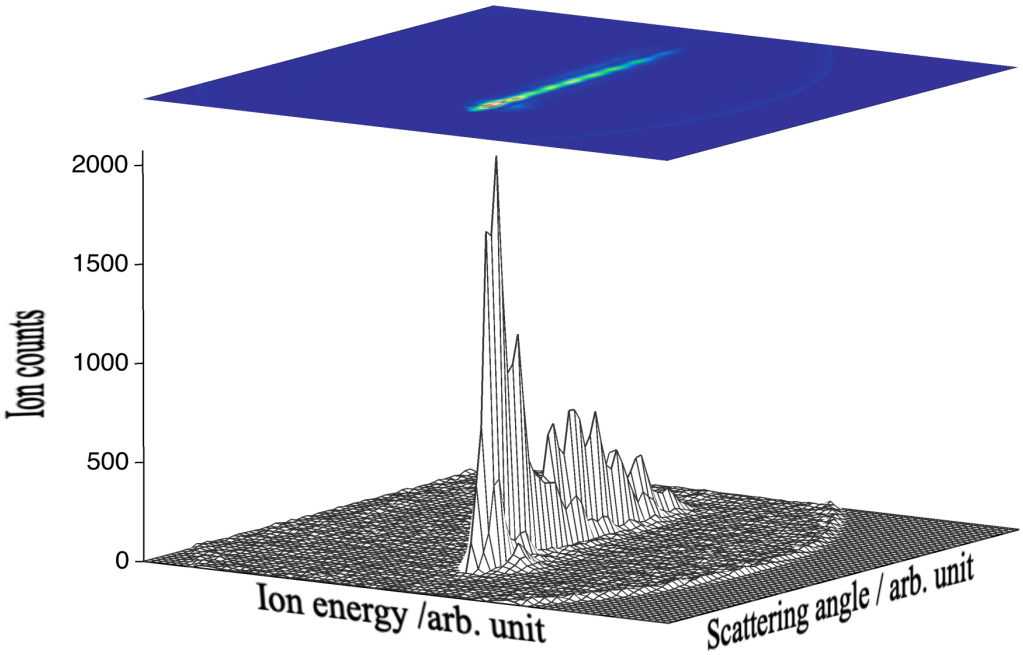


Fig. 1. (Color online) Example of the measured spectrum shown in a 3D graph. The elastically scattered ions in the $^{3}He^{+}$ – ^{4}He system at E_{lab} = 28 eV were recorded as a function of the energy and scattering angle.

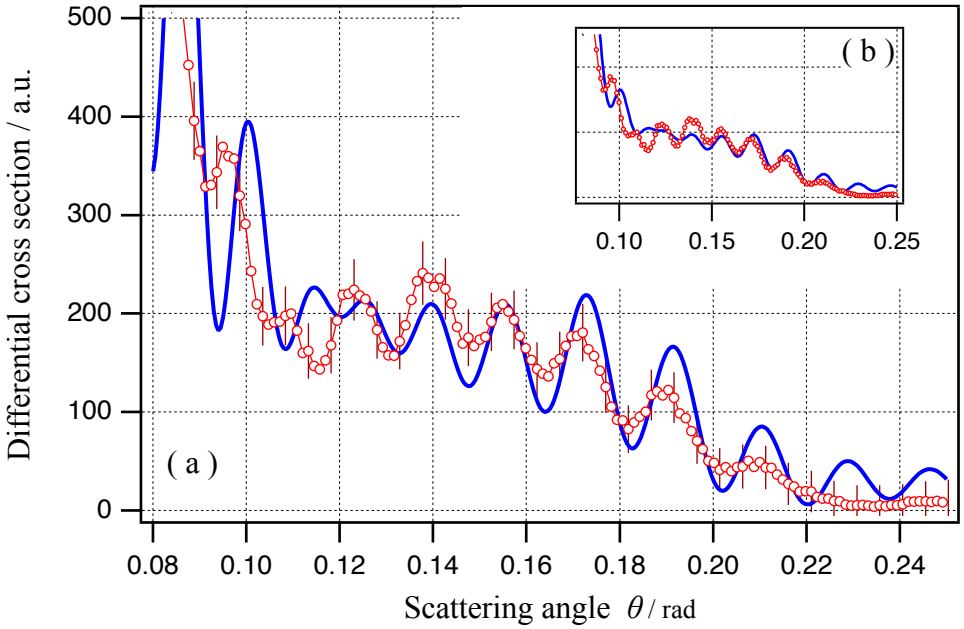


Fig. 2. (Color online) Measured and calculated DCSs for the elastic scattering in the $^3He^+ - {}^4He$ system. (a) Circles correspond to the measured DCS at $E_{lab} = 28$ eV converted to the cm coordinate, and the solid curve to the calculated DCS at $E_{lab} = 29$ eV. The measured relative DCS is scaled to the calculated value at about $\theta = 0.155$ rad. (b) Circles: the same as (a). The solid curve shows the calculated DCS at $E_{lab} = 29$ eV convoluted with the angular resolution of the present setup, about 0.25° (FWHM) in the lab frame.

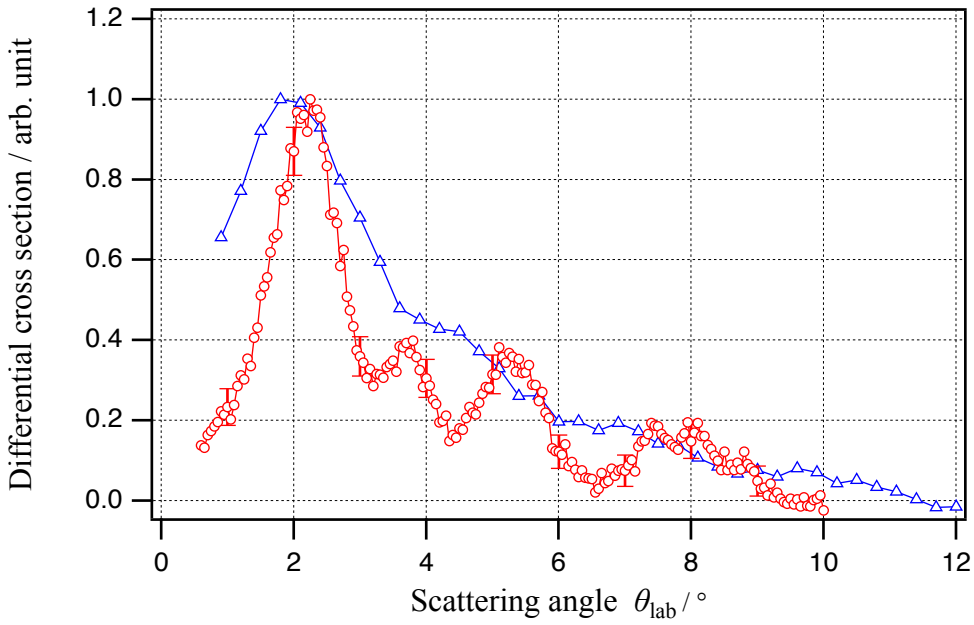


Fig. 3. (Color online) Measured DCSs for the reaction O^{2+} ($2s^2 2p^2\ ^3P$) + He ($1s^2\ ^1S$) → O^+ ($2s^2 2p^3\ ^2P$) + He^+ ($1s\ ^2S$) + 5.52 eV at E_{lab} = 48 eV. Circles correspond to the present measurements, and triangles to the previously reported DCS at E_{lab} = 50 eV.[3)] Both DCSs are scaled to unity at the peak position.

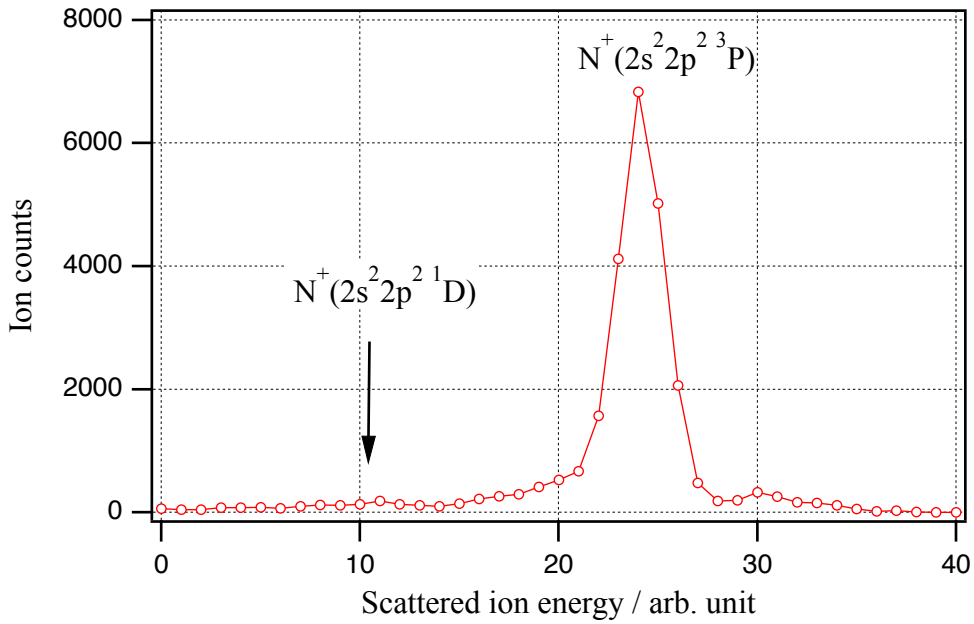


Fig. 4. (Color online) Energy spectrum of the scattered ion, N^+, produced in the reaction N^{2+} $(2s^2 2p\ ^2P)$ + He $(1s^2\ ^1S) \rightarrow N^+ (2s^2 2p^2\ ^3P)$ + $He^+ (1s\ ^2S)$ + 5.01eV at E_{lab} = 48 eV. An arrow indicates the energy position of N^+ ion for the channel N^{2+} $(2s^2 2p\ ^2P)$ + He $(1s^2\ ^1S) \rightarrow N^+ (2s^2 2p^2\ ^1D)$ + $He^+ (1s\ ^2S)$ + 3.12 eV.

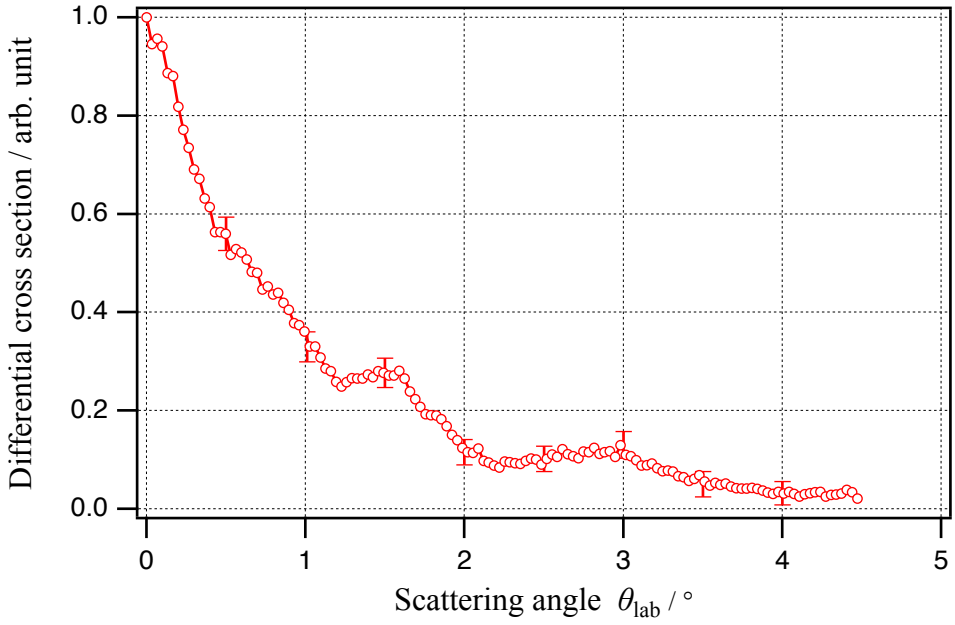


Fig. 5. (Color online) Measured DCS for the reaction N^{2+} ($2s^2 2p\ ^2P$) + He ($1s^2\ ^1S$) → N^+ ($2s^2 2p^2\ ^3P$) + He^+ ($1s\ ^2S$) + 5.01eV at E_{lab} = 48 eV. The peak position is scaled to unity.

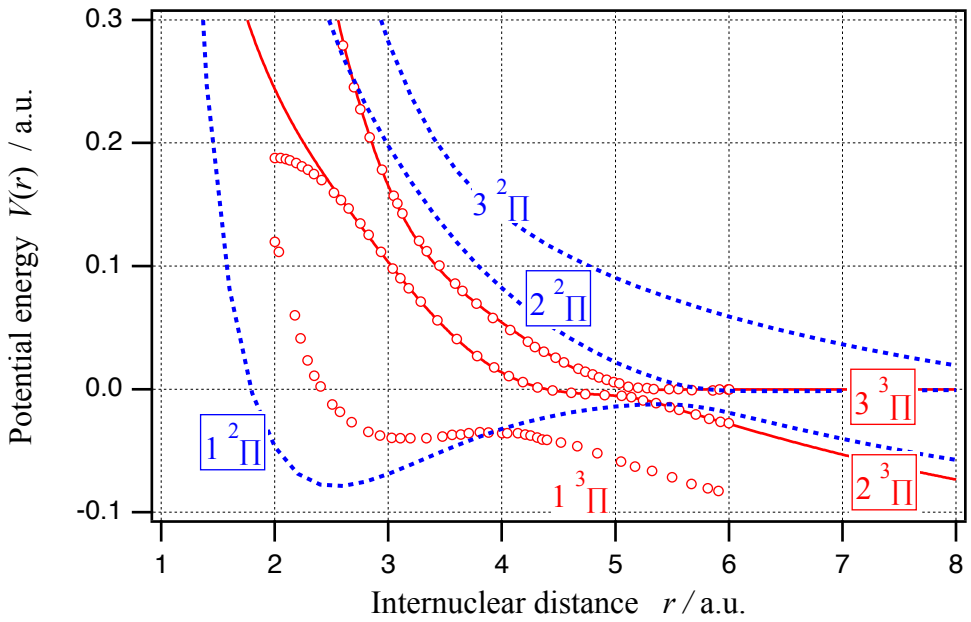


Fig. 6. (Color online) Interaction potentials used to calculate DCSs. Circles indicate the potential values for the O^{2+} – He system reported by Butler et al.[7] Solid curves indicate the fitted potentials for the use of DCS calculations. Dashed curves represent the fitted potentials for the N^{2+} – He system reported by Itoh and Ohtsuki. [14]

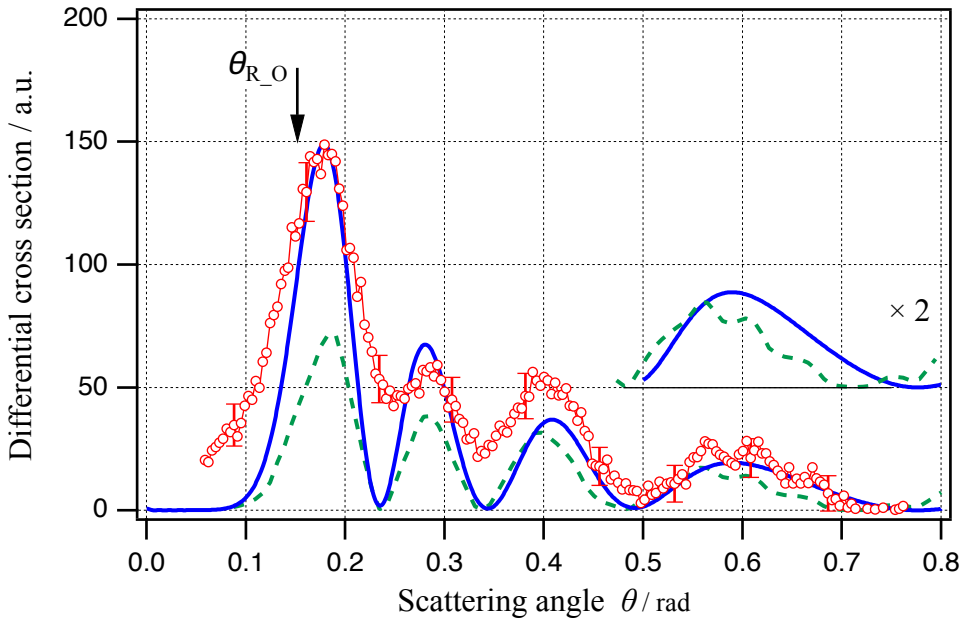


Fig. 7. (Color online) Calculated and measured DCSs for the reaction O^{2+} ($2s^2 2p^2\ ^3P$) + He ($1s^2\ ^1S$) → O^+ ($2s^2 2p^3\ ^2P$) + He^+ ($1s\ ^2S$) + 5.52 eV at E_{lab} = 48 eV. The solid curve represents the present calculated results. The dashed curve corresponds to the DCS calculated by Heil and Sharma.[6)] Circles represent the measured DCS converted to the cm coordinate. The measured DCS is scaled to the current calculated value at about θ = 0.18 rad. The rainbow angle θ_{R_O} is shown by the arrow (see text).

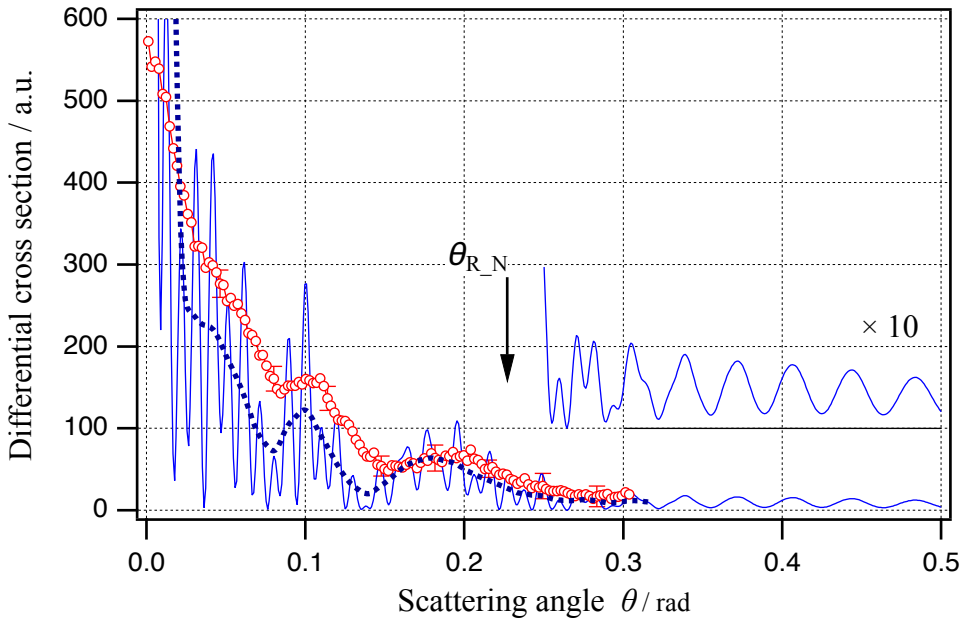


Fig. 8. (Color online) Calculated and measured DCSs for the reaction N^{2+} ($2s^2 2p\ ^2P$) + He → N^+ ($2s^2 2p^2\ ^3P$) + He^+ + 5.01 eV at E_{lab} = 48 eV. The solid curve represents the present calculated results. Circles represent the measured DCS converted to the cm coordinate. The measured DCS was scaled to the calculated value at about θ = 0.2 rad. The broken curve shows the calculated values convoluted with the experimental angular resolution. The rainbow angle θ_{R_N} is indicated by the arrow (see text).

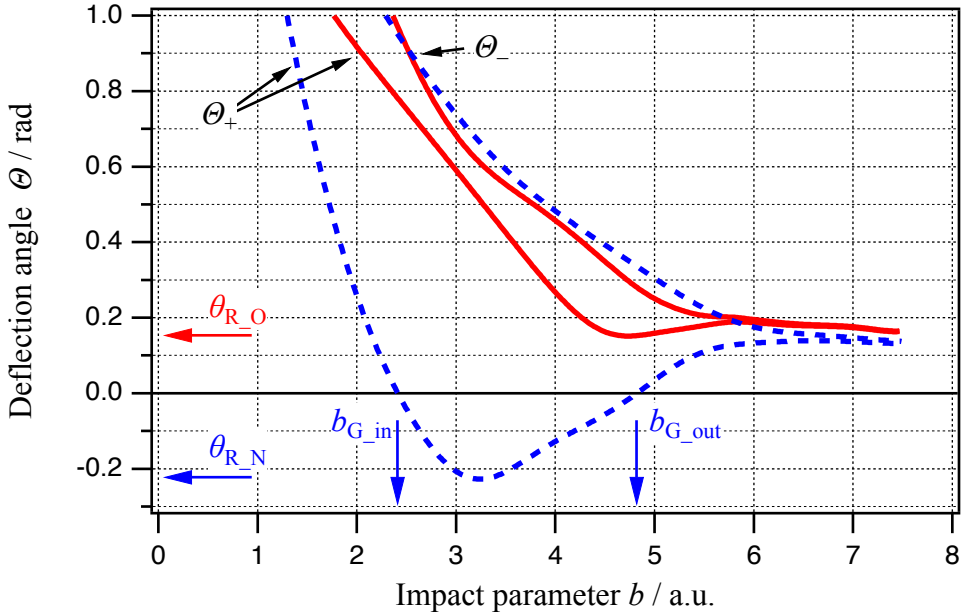


Fig. 9. (Color online) Deflection functions Θ_+ and Θ_-. The solid curves correspond to the reaction O^{2+} ($2s^2 2p^2\ ^3P$) + He ($1s^2\ ^1S$) → O^+ ($2s^2 2p^3\ ^2P$) + He^+ ($1s\ ^2S$) + 5.52 eV at E_{lab} = 48 eV, and the dashed curves to N^{2+} ($2s^2 2p\ ^2P$) + He → N^+ ($2s^2 2p^2\ ^3P$) + He^+ ($1s\ ^2S$) + 5.01 eV at E_{lab} = 48 eV. Rainbow angles, θ_{R_O}, θ_{R_N}, and impact parameters for the forward glory scattering, b_{G_in}, b_{G_out}, are shown by arrows (see text).